

Tensor Network Compression for Fully Spectral Vlasov–Poisson Simulation

Erik M. Åsgrim, Luca Pennati, Marco Pasquale, Stefano Markidis

KTH Royal Institute of Technology, Stockholm, 114 28, Sweden

Abstract

We propose a numerical method for kinetic plasma simulation in which the phase-space distribution function is represented by a low-rank tensor network with an adaptive level of compression. The Vlasov–Poisson system is advanced using Strang splitting, and each substep is treated spectrally in the corresponding variable. By expressing both the distribution function and the Fourier transform as tensor network objects (state and operator representations), spectral transforms are applied directly in compressed form, enabling time stepping without reconstructing the full phase-space grid. The self-consistent electric field is also computed within the tensor formalism. The charge density is obtained by contracting over velocity degrees of freedom and extracting the zero Fourier mode, which provides the source term for a spectral Poisson solver. We validate the approach on standard benchmarks, including Landau damping and the two-stream instability. Finally, we systematically study how compression parameters, including truncation tolerances and internal ranks (bond dimensions), affect momentum and energy conservation, positivity behavior, robustness to filamentation, and computational cost.

Keywords: Vlasov–Poisson equation, Kinetic plasma simulation, Tensor networks, Tensor train (TT), Matrix product state (MPS), Low-rank compression, Tensor cross interpolation (TCI)

1. Introduction

Plasma simulation models are essential for understanding and predicting plasma dynamics across a wide range of settings, from space and astrophysical environments [1] to magnetic confinement fusion [2] and accelerator-based technologies [3]. A variety of numerical descriptions are used in practice. Fluid models treat the plasma as a continuum and evolve macroscopic moments such as density, momentum, and energy [4, 5]. Kinetic models are more fundamental. They evolve the phase-space distribution function, which encodes the statistical density of particles as a function of position and velocity [6]. In many regimes of interest, collisional effects are negligible on the timescales under consideration, and the distribution function evolves according to the collisionless Vlasov equation. The plasma dynamics are driven by self-consistent electromagnetic fields governed by Maxwell’s equations, or by the Poisson equation in the electrostatic limit [3]. This leads to a nonlinear coupling. The force term in the Vlasov equation depends on fields determined by moments of the distribution function, while those moments are obtained by integrating the evolving distribution over velocity.

A primary numerical challenge in kinetic plasma simulation is the cost of representing the phase-space distribution function [7, 8]. In a standard Eulerian discretization, both physical space and velocity space are sampled on grids [9, 10]. While spatial resolution can often be managed with established discretization and parallelization strategies, accurately resolving velocity-space structure is substantially more demanding. Phase mixing and filamentation generate increasingly fine features that require very high resolution [9, 10]. The situation becomes prohibitive in the full six-dimensional phase space, where the number of degrees of freedom grows exponentially with dimension, exemplifying the *curse of dimensionality* [11]. For this reason, many Vlasov solvers employ adaptive or problem-dependent strategies for velocity-space discretization [12, 13]. An alternative is to introduce a compressed representation of the distribution function and formulate the governing equations directly in that compressed space, avoiding repeated encoding and decoding of a full grid-based state [14]. Particle-in-Cell (PIC) methods can be viewed as one such compression strategy: the distribution is represented by a finite set of macroparticles, and the kinetic dynamics are advanced along characteristics [15, 16]. This representation is inherently lossy and introduces sampling noise. Regions of phase space that are poorly populated by particles may be inaccurately represented, and small-amplitude

features can be missed without very large particle counts.

In this study, we pursue a compression paradigm based on low-rank factorization of the phase-space distribution function [17, 14, 18]. Specifically, we adopt techniques originally developed for the numerical simulation of many-body quantum systems and represent the distribution function using a tensor network. This representation can be made exact up to floating-point accuracy when truncation is disabled, or used in a controlled approximate mode by truncating internal ranks [18]. We evolve the Vlasov–Poisson system using operators expressed in the same compressed formalism so that the full phase-space distribution never needs to be explicitly reconstructed. This approach offers three key advantages. First, tensor networks provide a compressed low-rank representation of high-dimensional data, with the potential to reduce storage and computational costs by orders of magnitude when the underlying solution exhibits a suitable low-rank structure. Although no general guarantees exist that a given Vlasov solution admits such compression uniformly in time, a growing body of empirical evidence indicates that many physically relevant kinetic problems possess an intrinsic, approximately low-rank structure in appropriate representations [19, 20, 21, 22, 23]. Second, the tensor network framework allows the compression level to be tuned adaptively, ranging from essentially lossless representations (up to floating-point accuracy when no truncation is applied) to controlled lossy approximations via rank truncation. This offers an alternative to particle-based compression strategies while retaining the possibility of high-accuracy solutions. Third, the tensor network formalism enables the governing equations to be expressed and advanced directly in compressed form, avoiding repeated reconstruction of the full phase-space state. When both the state and the relevant operators admit low-rank tensor network representations, linear maps can be applied efficiently through structured tensor contractions. An important example is the Fourier transform. It was first observed empirically to admit a highly compressible matrix product operator representation [24] and later established analytically [25], enabling efficient spectral transforms in high-dimensional settings.

Tensor network methods, and in particular the tensor train (TT) representation (a chain-structured tensor network, also known as a matrix product state, MPS), have emerged as an effective framework for the numerical simulation of high-dimensional dynamical systems. Originally developed for compact representations of quantum many-body states [26, 27, 28, 29], these ideas have since been adapted into a broader class of *quantum-inspired* meth-

ods for classical computation. In this setting, notions such as entanglement and state compression are reinterpreted as low-rank structure and controllable approximation in exponentially large spaces, providing a scalable algebraic toolbox for high-dimensional problems [30, 31]. TT-based techniques have consequently been applied to a wide range of classical dynamical systems [32, 33], including fluid dynamics [20, 34, 35, 36], the Fokker–Planck equation [37], transport problems [38], and nonlinear wave equations such as the Gross–Pitaevskii equation [23]. In kinetic plasma simulation, TT-based solvers have been proposed for the Vlasov–Poisson system using semi-Lagrangian schemes [19] as well as explicit time integrators combined with tensor-structured finite-difference operators [39]. Extensions to more general plasma models, including Vlasov–Maxwell systems, have also been investigated [40, 41].

In this work, we introduce a spectral Vlasov–Poisson solver in which the phase-space distribution function f is represented in the TT format. Our method adopts a fully spectral discretization in each variable. Time integration is performed with a second-order Strang splitting scheme [42], so that the advection and acceleration substeps can be advanced efficiently in Fourier space while remaining within the TT formalism. The advection substep is realized through the application of structured Fourier-space operators represented as matrix product operators, leading to efficient tensor contractions. The acceleration step, driven by the self-consistent electric field, is treated by reconstructing the updated tensor network state via tensor cross interpolation (TCI) [43, 44] from pointwise evaluations of the split-step update. This strategy follows and extends recent tensor network spectral time-evolution techniques developed for nonlinear Schrödinger-type dynamics [23]. Numerical experiments show that the proposed solver reproduces standard benchmarks, including Landau damping and the two-stream instability, while achieving substantial compression and favorable computational scaling relative to uniform-grid spectral methods.

This paper is organized as follows. Section 2 introduces the required theoretical background, including a review of splitting integration methods of the Vlasov–Poisson equation and the *quantics tensor train* encoding of the distribution function. In Section 3, we describe the spectral TT-based Vlasov–Poisson solver developed in this work. Sections 3.1–3.2 detail the underlying theoretical formulation, while Sections 3.3 and 3.4 address computational complexity and implementation aspects. Numerical results obtained with the spectral TT-based solver are presented in Section 4, with Landau

damping and the two-stream instability serving as benchmark problems. Section 5 analyzes these results, highlighting both the strengths and limitations of the method and outlining directions for future work. Concluding remarks are given in Section 6.

2. Preliminaries

2.1. Spectral splitting scheme of the Vlasov–Poisson equation

The one-dimensional electron phase-space distribution function $f(x, v, t)$ in the presence of a static, uniform neutralizing background field is governed by the 1D1V Vlasov–Poisson equation

$$\partial_t f + v \partial_x f - E(x) \partial_v f = 0 \quad (1)$$

$$\partial_x E = 1 - \int_{-\infty}^{\infty} f(x, v, t) dv \quad (2)$$

where the charge-mass ratio is set to $q/m = -1$ for convenience.

The Vlasov–Poisson equation can be numerically integrated by employing a splitting scheme, which relies on separating the advection and acceleration of Eq. (1) into two distinct subproblems [42, 45, 10]. By defining the transport operators $\hat{\mathcal{A}} = -v \partial_x$ and $\hat{\mathcal{B}} = E(x) \partial_v$, the advection and acceleration subproblems can be formulated as

$$\begin{cases} \partial_t f = \hat{\mathcal{A}} f, & \text{(advection)} \\ \partial_t f = \hat{\mathcal{B}} f, & \text{(acceleration).} \end{cases} \quad (3)$$

After Fourier transforming in the variable of differentiation, the time evolution generated by $\hat{\mathcal{A}}$ and $\hat{\mathcal{B}}$ reduces to diagonal phase shift operators in Fourier space. Denoting by $\hat{\mathcal{F}}_x$ and $\hat{\mathcal{F}}_v$ the Fourier transforms in space and velocity, the exact solutions of the two subproblems over a time increment Δt can be written as

$$\begin{cases} f(x, v, t + \Delta t) = \underbrace{\hat{\mathcal{F}}_x^{-1} \exp(-ik_x v \Delta t) \hat{\mathcal{F}}_x}_{{\mathcal{S}}_{\text{adv}}(\Delta t)} f(x, v, t), & \text{(advection),} \\ f(x, v, t + \Delta t) = \underbrace{\hat{\mathcal{F}}_v^{-1} \exp(ik_v E(x) \Delta t) \hat{\mathcal{F}}_v}_{{\mathcal{S}}_{\text{acc}}(\Delta t; E)} f(x, v, t), & \text{(acceleration).} \end{cases} \quad (4)$$

Here $k_x = 2\pi n_x / (x_{\max} - x_{\min})$ and $k_v = 2\pi n_v / (v_{\max} - v_{\min})$ denote the discrete Fourier wavenumbers associated with the spatial and velocity grids, respectively, with n_x and n_v denoting the integer mode indices. The Fourier representation assumes periodic boundary conditions in the transformed variable. While periodicity in space is physical, periodicity in velocity is a numerical artifact introduced by truncating the velocity domain. Hence, we must choose a sufficiently large velocity interval such that the distribution function remains negligible near the velocity boundaries.

Time evolution according to the splitting scheme proceeds by alternately evolving the state $f(x, v, t)$ under the advection and acceleration generators. Using the update rules in Eq. (4), we utilize a second-order Strang splitting scheme [42]. The solution is advanced from t^n to $t^{n+1} = t^n + \Delta t$ by sequentially executing the following set of operations

$$f^{(1)} = \hat{\mathcal{F}}_x^{-1} \exp(-ik_x v \Delta t / 2) \hat{\mathcal{F}}_x f^n, \quad (5)$$

$$f^{(2)} = \hat{\mathcal{F}}_v^{-1} \exp(ik_v E^{(1)}(x) \Delta t) \hat{\mathcal{F}}_v f^{(1)}, \quad (6)$$

$$f^{n+1} = \hat{\mathcal{F}}_x^{-1} \exp(-ik_x v \Delta t / 2) \hat{\mathcal{F}}_x f^{(2)}. \quad (7)$$

where $f^{(1)}$ and $f^{(2)}$ denote intermediate states, and the electric field $E^{(1)}(x)$ used in the acceleration step is computed self-consistently from $f^{(1)}$.

When this splitting scheme is applied repeatedly, the final half-advection of one time step and the initial half-advection of the subsequent step can be merged. Over N_s time steps, the evolution may therefore be written compactly as

$$f^{N_s} = \mathcal{S}_{\text{adv}}\left(\frac{\Delta t}{2}\right) \mathcal{S}_{\text{acc}}(\Delta t; E) [\mathcal{S}_{\text{adv}}(\Delta t) \mathcal{S}_{\text{acc}}(\Delta t; E)]^{N_s-1} \mathcal{S}_{\text{adv}}\left(\frac{\Delta t}{2}\right) f^0, \quad (8)$$

where \mathcal{S}_{adv} and \mathcal{S}_{acc} denote the advection and acceleration update operators defined in Eq. (4). We graphically depict the spectral splitting integration scheme of Eq. (8) in Fig. 1.

2.2. Compressed tensor representation of the phase-space distribution

It is possible to encode functions, such as the phase-space distribution function $f(x, v)$, in a compressed tensor format using the so-called *quantics tensor train* representation [46, 32].

We consider the distribution function $f(x, v)$ defined on a rectangular domain $x \in [x_{\min}, x_{\max}]$ and $v \in [v_{\min}, v_{\max}]$, and discretize both spatial and velocity dimensions using uniform grids with 2^R internal points each. A direct

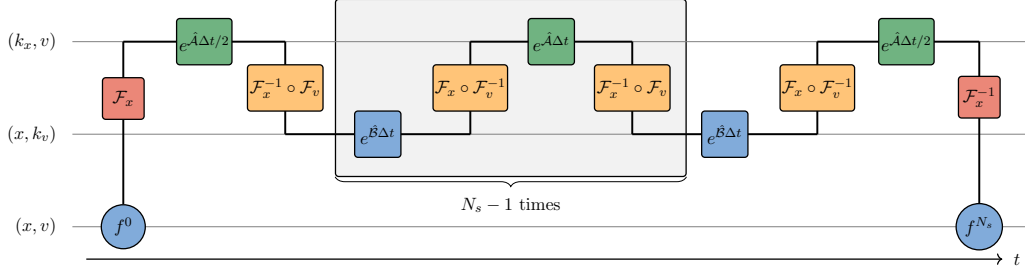


Figure 1: Workflow for the spectral Strang splitting integration scheme described in Eq. (8) over N_s time steps. For both advection and acceleration, the solution is transformed to the Fourier domain of the variable of differentiation, after which the corresponding time propagator is applied. The highlighted block indicates the repeated inner loop applied $N_s - 1$ times.

representation of the resulting $2^R \times 2^R$ array quickly becomes infeasible for large R , as both memory and computational costs scale exponentially. The quantics approach circumvents this issue by expressing each grid index in binary form,

$$i_x = (b_1^{(x)}, \dots, b_R^{(x)}), \quad i_v = (b_1^{(v)}, \dots, b_R^{(v)}), \quad (9)$$

with $b_k^{(x)}, b_k^{(v)} \in \{0, 1\}$. The discretized distribution function $f(x_{i_x}, v_{i_v})$ can then be viewed as a tensor $F_{b_1^{(x)} b_1^{(v)} \dots b_R^{(x)} b_R^{(v)}}$ of order $N = 2R$, where each index corresponds to a single binary digit.

This high-order tensor is represented in *tensor train* (TT) format as a chain of low-rank tensors connected by a set of auxiliary indices,

$$F_{b_1^{(x)} b_1^{(v)} \dots b_R^{(x)} b_R^{(v)}} = \sum_{\{\alpha\}} A_{b_1^{(x)} \alpha_1}^{(1)} A_{\alpha_1 b_1^{(v)} \alpha_2}^{(2)} \dots A_{\alpha_{2R-2} b_R^{(x)} \alpha_{2R-1}}^{(2R-1)} A_{\alpha_{2R-1} b_R^{(v)}}^{(2R)} \quad (10)$$

effectively factorizing the full tensor $F_{b_1^{(x)} b_1^{(v)} \dots b_R^{(x)} b_R^{(v)}}$ (see Fig. 2(a)). Here, each local tensor $A^{(k)}$ carries one binary *site index* and two auxiliary *bond indices*, whose dimension χ controls the amount of compression. While the full tensor $F_{b_1^{(x)} b_1^{(v)} \dots b_R^{(x)} b_R^{(v)}}$ contains $\mathcal{O}(2^N)$ entries, its TT representation requires storing only $\mathcal{O}(N\chi^2)$ entries, hence giving exponential compression, provided that the bond dimensions remain bounded.

Crucially, the tensor cross interpolation (TCI) algorithm allows us to construct a compressed TT representation of the discretized distribution function $f(x_{i_x}, v_{i_v})$ without having to store the full exponentially large tensor

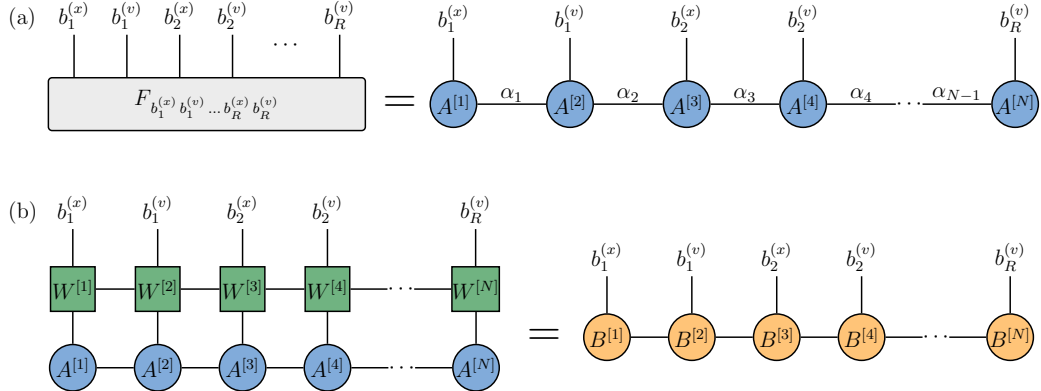


Figure 2: **(a)** The discretized distribution function $f(x_{i_x}, v_{i_v})$ is encoded as a rank- $2R$ tensor using the quantics representation and subsequently compressed into a tensor train (TT) format. In a tensor network diagram, nodes denote tensors, while edges connecting two nodes indicate summation (contraction) over a shared index. Edges that terminate without connecting to another node represent free (site) indices of the tensor. **(b)** Application of a matrix product operator (MPO) to the TT representation of f , yielding a new TT with the same physical structure. The action of the MPO is performed by contracting the site indices of the TT with the corresponding input indices of the MPO at each site.

$F_{b_1^{(x)} b_1^{(v)} \dots b_R^{(x)} b_R^{(v)}}$ [18, 47, 44]. Instead, TCI assumes oracle access (black-box access to tensor entries on demand) to the tensor $F_{b_1^{(x)} b_1^{(v)} \dots b_R^{(x)} b_R^{(v)}}$, and provides an approximate TT representation of the full tensor by querying only $\mathcal{O}(Nd\chi^2)$ tensor entries. For a detailed discussion of the TCI algorithm, we refer to the overview provided in [44].

Although the ordering of the binary indices within the TT is, in principle, arbitrary, the choice of ordering can have a significant impact on the size of the bond dimensions in the compressed TT state [39]. In this work, we employ an *interleaved* ordering in which bits corresponding to position and velocity alternate along the TT chain. This choice places bits encoding comparable physical scales at neighboring sites, allowing the TT representation to efficiently capture correlations between position and velocity across scales.

A key advantage of the TT formalism is that linear operators acting on TT-encoded functions can themselves be represented in a compressed tensor network form, referred to as *matrix product operators* (MPO), enabling their efficient application while remaining entirely within the tensor framework. Operators such as Fourier transforms can be applied efficiently through tensor contractions (see Fig. 2 (b)), a property that is central to the spectral solver

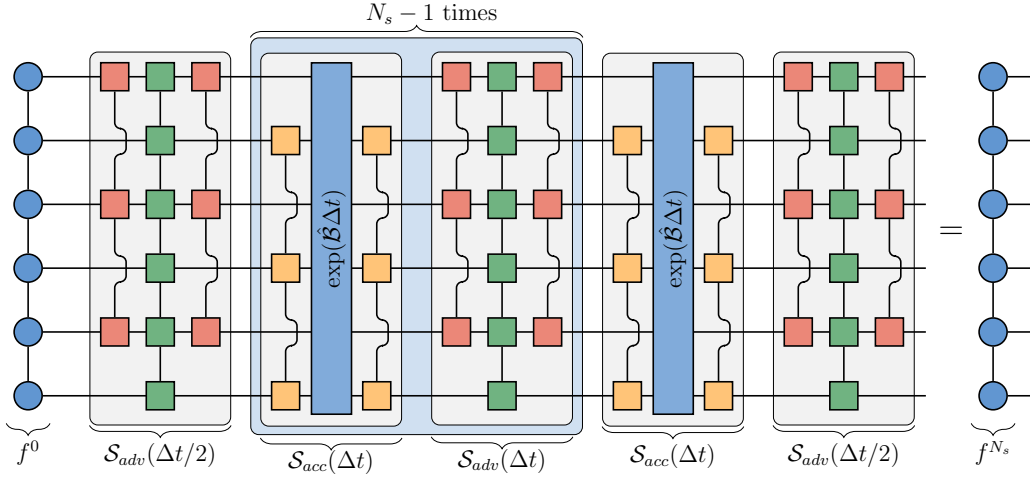


Figure 3: Time evolution of the TT representation of the initial condition f^0 , following the sequence dictated by the second-order Strang splitting scheme. Advection steps are implemented via TT–MPO contractions, whereas the acceleration steps are realized using tensor cross interpolation (TCI). Fourier transforms in position (red) and velocity (yellow) act only on the corresponding TT site registers, whereas the phase shifts associated with advection and acceleration (green and blue) act on the full position–velocity register.

developed in this work.

3. Spectral tensor train Vlasov–Poisson solver

3.1. Time evolution within the tensor train framework

The discrete Fourier transforms in position and velocity required for the spectral splitting scheme, together with their inverses, are implemented using the analytic MPO construction introduced by Chen et al. [25], which requires only a bond dimension of $\chi \approx 11$ for machine precision. Throughout this work, we employ a unitary normalization of the discrete Fourier transform, with both the forward and inverse transforms carrying a prefactor of $1/\sqrt{2^R}$. The Fourier transforms act only on the subset of R sites of the TT associated with either the position or velocity register. To embed the Fourier MPOs into the full position–velocity register, we insert identity operators on all sites corresponding to the complementary coordinate. An important aspect of the compressed MPO representation of the Fourier transform is that it reverses the order of the quantics bit register. As a result, subsequent operations

in spectral Fourier space are carried out with respect to this reversed bit ordering.

To construct the MPO representation of the advection propagator $\exp(\hat{\mathcal{A}}\Delta t)$, we exploit the fact that $\hat{\mathcal{A}} = -v \partial_x$ is diagonal in the Fourier representation with respect to the spatial coordinate. Conjugation with the spatial Fourier transform yields

$$\exp(\Delta t \hat{\mathcal{A}}) = \hat{\mathcal{F}}_x^{-1} \exp(-ik_x v \Delta t) \hat{\mathcal{F}}_x, \quad (11)$$

such that time evolution under $\hat{\mathcal{A}}$ reduces to pointwise multiplication by a scalar phase factor in (k_x, v) -space. Since the distribution function is represented on a quantics grid, this phase factor can be viewed as a scalar-valued function defined on the same grid and approximated in TT format. In particular, we approximate the phase factor $\exp(-ik_x v \Delta t)$ by a TT on the quantics grid using TCI. This yields a TT representation

$$G_{\tilde{b}_1^{(x)} \tilde{b}_1^{(v)} \dots \tilde{b}_R^{(x)} \tilde{b}_R^{(v)}} = \sum_{\{\alpha\}} B_{\tilde{b}_1^{(x)} \alpha_1}^{(1)} B_{\alpha_1 \tilde{b}_1^{(v)} \alpha_2}^{(2)} \dots B_{\alpha_{2R-2} \tilde{b}_R^{(x)} \alpha_{2R-1}}^{(2R-1)} B_{\alpha_{2R-1} \tilde{b}_R^{(v)}}^{(2R)}, \quad (12)$$

which represents the phase shift acting pointwise on the quantics grid.

The corresponding MPO \mathcal{M} is obtained by promoting the scalar TT in Eq. (12) to a diagonal operator through contraction with three-index Kronecker deltas, enforcing the equality of input and output indices at each site:

$$\mathcal{M}_{b_1^{(x)} b_1^{(v)} \dots b_R^{(x)} b_R^{(v)}; b_1^{(x)\prime} b_1^{(v)\prime} \dots b_R^{(x)\prime} b_R^{(v)\prime}} = \sum_{\{\tilde{b}\}} G_{\tilde{b}_1^{(x)} \tilde{b}_1^{(v)} \dots \tilde{b}_R^{(x)} \tilde{b}_R^{(v)}} \prod_{r=1}^R \delta_{b_r^{(x)} b_r^{(x)\prime} \tilde{b}_r^{(x)}} \delta_{b_r^{(v)} b_r^{(v)\prime} \tilde{b}_r^{(v)}}. \quad (13)$$

Contracting the MPO \mathcal{M} with a TT has the desired effect of multiplying by $\exp(-ik_{i_x} v_{i_v} \Delta t)$ pointwise on the quantics grid. In Eq. (13), we associate the input (output) indices with the unprimed (primed) indices.

Crucially, the advection MPO is time-independent and needs to be constructed only once. Following [23], we control the bond dimension of the resulting MPO by applying a spectral filter to the phase factor,

$$\hat{\Theta}(k) = \frac{1}{\exp((|k| - k_{\max})\beta) + 1}, \quad (14)$$

and construct the filtered operator $\hat{\Theta}(k_{i_x}) \exp(-ik_{i_x} v_{i_v} \Delta t)$. Here, k_{\max} determines the maximum retained mode, while β controls the sharpness of the cutoff.

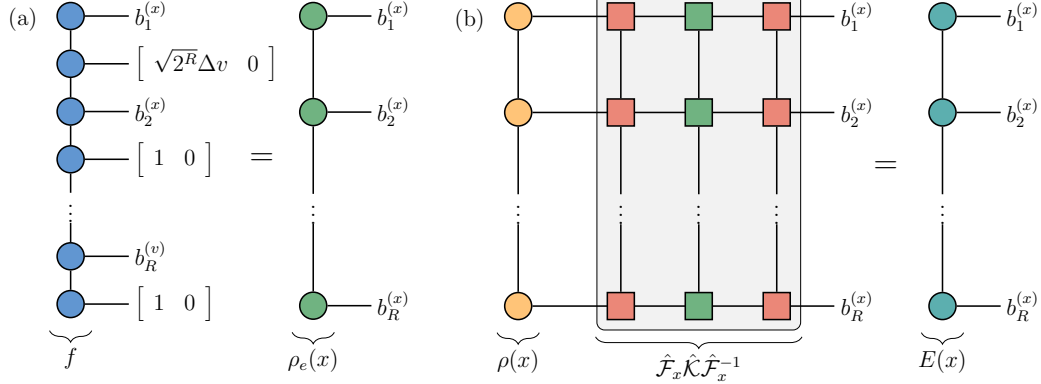


Figure 4: (a) The electron density ρ_e is computed by contracting the tensors in the velocity register by $[1 \ 0]^T$, effectively selecting the zero-mode. One site must be contracted by $[\sqrt{2R} \Delta v \ 0]^T$, to consider the spacing of the spatial grid and to compensate for the prefactor of the unitary Fourier transform. (b) The electric field is acquired by multiplying the TT representation of the charge density ρ by a sequence of three MPOs, corresponding to Eq. (18).

For the acceleration step, the induced phase factor $\exp(iE(x_{i_x})k_{i_v}\Delta t)$ depends explicitly on the electric field and therefore changes at every time step. In this case, we do not construct an MPO and instead directly apply TCI to approximate the evolved state in the Fourier basis

$$\hat{f}'(x_{i_x}, k_{i_v}) = \hat{\Theta}(k_{i_v}) \exp(iE(x_{i_x})k_{i_v}\Delta t) \hat{f}(x_{i_x}, k_{i_v}), \quad (15)$$

by querying the right-hand side of Eq. (15). By directly fitting the evolved state rather than constructing an acceleration MPO, we circumvent the need to execute an additional TT–MPO contraction. Due to the time dependence of the self-induced electric field, a new TCI fit must be computed at each time step. We provide a discussion on the computational cost and scaling of the algorithm in Section 3.3.

Notably, after each time step we rescale the TT entries to ensure that the total charge remains conserved throughout the simulation.

3.2. Computing the electric field

To carry out the acceleration step in Eq. (6) of the splitting scheme, the electric field must be computed from the TT representation of the state f . As described below, this can be accomplished while remaining entirely within the tensor framework.

We first compute the electron density $\rho_e(x_{i_x})$ by summing the distribution function over the velocity domain

$$\rho_e(x_{i_x}) = \sum_{i_v} f(x_{i_x}, v_{i_v}) \Delta v, \quad (16)$$

where we let $\Delta v = (v_{\max} - v_{\min})/2^R$ denote the spacing of the velocity grid. Assuming that the velocity register of the quantics TT representing f is given in the Fourier basis, the summation corresponds to selecting the zero Fourier mode. Because a unitary discrete Fourier transform is used, the zero mode equals the velocity sum divided by $\sqrt{2^R}$. The density extraction therefore amounts to contracting each velocity site with the rank-1 tensor $[1 \ 0]^T$, except for a single site that is contracted with $[\sqrt{2^R} \Delta v \ 0]^T$. The resulting object is a rank- R TT defined solely over the spatial register, representing the spatial electron density $\rho_e(x_{i_x})$. A schematic of the tensor contraction is shown in Fig. 4(a).

Including a uniform ion background with unit density, the total charge density is then given by

$$\rho(x_{i_x}) = 1 - \rho_e(x_{i_x}). \quad (17)$$

The electric field is obtained by solving the Poisson equation (2) in Fourier space

$$E(x_{i_x}) = \hat{\mathcal{F}}_x^{-1} \hat{\mathcal{K}}(k_{i_x}) \hat{\mathcal{F}}_x \rho(x_{i_x}), \quad \hat{\mathcal{K}}(k_x) = \begin{cases} -\frac{i}{k_x}, & k_x \neq 0, \\ 0, & k_x = 0, \end{cases} \quad (18)$$

where the zero mode $k_x = 0$ is set to zero to enforce a zero-mean electric field. The Fourier-space multiplier $\hat{\mathcal{K}}(k_x)$ is represented as an MPO constructed using TCI, following the same methodology employed for the advection propagator described previously in Section 3.1. The quantics TT representation of the electric field is then acquired through a sequence of TT-MPO contractions, as illustrated in Fig. 4(b).

3.3. Complexity analysis

Constructing the analytic Fourier MPOs of the position and velocity registers scale as $\mathcal{O}(N^2 \chi^3)$, with $N = 2R$ denoting the total number of site indices [25]. This cost is incurred only once for a given quantics grid and is

therefore a preprocessing step that does not add to the per-time-step runtime of the algorithm.

Fitting the MPO that represents the phase shift induced by advection using TCI scales as $\mathcal{O}(Nd\chi^3)$ [44, 47], where χ denotes the maximum bond dimension of the resulting tensor and $d = 2$ is the dimension of the binary site indices. As in the case of the Fourier MPOs, the advection MPO depends only on the chosen quantics grid and therefore needs to be constructed only once. The same $\mathcal{O}(Nd\chi^3)$ scaling applies to the TCI fit used to obtain the evolved state after the acceleration step in Eq. (15). However, since this fit is performed once every time step, it constitutes a recurring contribution to the total computational cost.

The TT–MPO contractions required to perform the Fourier transforms and advection time evolution on the state f scale as $\mathcal{O}(Nd^2\chi_{\text{TT}}^2\chi_{\text{MPO}}^2)$, where we let χ_{TT} and χ_{MPO} denote the maximum bond dimensions of the TT and MPO, respectively [28, 48]. The resulting TT has a bond dimension given by the product $\chi_{\text{TT}}\chi_{\text{MPO}}$, which is why each TT–MPO contraction is followed by a truncation of the bond dimension back to χ_{TT} . The contraction procedure is initialized by moving the orthogonality center to the right-most TT site using a QR decomposition sweep scaling as $\mathcal{O}(Nd\chi_{\text{TT}}^3\chi_{\text{MPO}}^3)$. Subsequently, we perform an SVD-sweep over all the TT sites in the opposite direction, truncating each bond throughout the sweep. The full truncation sweep scales as $\mathcal{O}(Nd^2\chi_{\text{TT}}^3\chi_{\text{MPO}})$. It is worth emphasizing that all steps scale linearly with respect to the number of bits $N = 2R$ used in the quantics representation. Hence, provided the bond dimension of the state f and the MPO operations remain bounded, we expect an exponential speed-up over conventional methods operating on the full $2^R \times 2^R$ grid.

3.4. Implementation details

We execute numerical simulations on a quantics grid using $R = 10$ bits for both the spatial and velocity dimensions, corresponding to 2^R grid points per dimension. In total, we therefore operate on a position-velocity grid with $2^{20} \approx 10^6$ grid points. Time integration is carried out using a fixed time step $\Delta t = 0.1$. The tolerance of the tensor cross interpolation (TCI) fits is fixed at $\tau = 10^{-8}$. The TCI tolerance corresponds to a sampled approximation of the relative L^∞ error of the fitted tensor evaluated on the adaptively queried tensor entries rather than on the full domain. The spectral filtering parameter k_{max} is set such that 2^7 discrete Fourier modes are retained and the cutoff sharpness is fixed at $\beta = 2$.

Table 1: Summary of numerical and algorithmic parameters used in generating the numerical results.

Parameter	Value
Quantics bits per dimension (x, v)	$R = 10$
Grid points per dimension	$2^R = 1024$
Total phase-space grid size	$2^{20} \approx 10^6$
Time step	$\Delta t = 0.1$
TCI tolerance	$\tau = 10^{-8}$
TT truncation cutoff	ϵ (varied)
Electric field max. bond dimension	$\chi_\varepsilon = 32$

Tensor-train truncation is controlled via a singular value decomposition (SVD) cutoff error ϵ . At each truncation step, the smallest singular values $\{\sigma_n\}$ are discarded such that the relative truncation error remains below ϵ , defined as

$$\frac{\sum_{n \in \text{discarded}} \sigma_n^2}{\sum_n \sigma_n^2} < \epsilon. \quad (19)$$

This truncation procedure is performed for each bipartition of the TT after every MPO contraction by performing a sweep over the full TT. For the TT representation of the electric field, a fixed maximum bond dimension of $\chi_\varepsilon = 32$ is imposed. A summary of the numerical and algorithmic parameters is provided in Table 1.

All simulations are implemented in **Julia** using the **ITensors.jl** library [49], coupled with the **TCI.jl** package [44] used to execute the TCI algorithm.

4. Numerical results

In this section, we assess the accuracy, stability, and computational behavior of the proposed TT-based spectral Vlasov–Poisson solver. The algorithm is assessed with standard 1D1V tests using Landau damping and the two-stream instability as complementary benchmarks. The TTs corresponding to the initial conditions are acquired via TCI. Unless otherwise stated, all simulations are performed using the fixed parameters specified in Table 1.

In evaluating the numerical protocol, we monitor the momentum P , the electric field energy $\mathcal{E}_{\text{field}}$, and the total energy $\mathcal{E} = \mathcal{E}_{\text{field}} + \mathcal{E}_{\text{kin}}$, where \mathcal{E}_{kin}

denotes the kinetic energy. Given the TT representation of the phase-space distribution $f(x_{i_x}, v_{i_v})$ and the electric field $E(x_{i_x})$, these quantities are computed in discretized form as

$$\begin{aligned} P &= \Delta x \Delta v \sum_{i_x, i_v} v_{i_v} f(x_{i_x}, v_{i_v}), \\ \mathcal{E}_{\text{field}} &= \frac{\Delta x}{2} \sum_{i_x} |E(x_{i_x})|^2, \\ \mathcal{E}_{\text{kin}} &= \frac{\Delta x \Delta v}{2} \sum_{i_x, i_v} v_{i_v}^2 f(x_{i_x}, v_{i_v}). \end{aligned} \quad (20)$$

with Δx and Δv denoting the position and velocity grid point spacing. All three observables are evaluated efficiently via tensor contractions within the TT formalism. We do not explicitly monitor charge conservation, as it is guaranteed by construction due to the active TT rescaling after each time step.

4.1. Physics validation

We first validate the solver by comparing the decay or growth rate of the first electric-field mode against analytical predictions in the linear regime. For both Landau damping and the two-stream instability, a single reference simulation is performed using a singular value truncation threshold of $\epsilon = 10^{-10}$.

Linear Landau damping. We simulate linear Landau damping on the phase-space domain $x \in [-2\pi, 2\pi]$ and $v \in [-6, 6]$. The initial distribution is set to a Maxwellian with a first Fourier-mode spatial perturbation,

$$f(x, v, 0) = \frac{1}{\sqrt{2\pi} v_{\text{th}}} \exp\left(-\frac{v^2}{2v_{\text{th}}^2}\right) (1 + A \cos(kx)), \quad k = \frac{2\pi}{L_x}, \quad (21)$$

with thermal velocity $v_{\text{th}} = 1.0$ and perturbation amplitude $A = 0.01$. For this standard benchmark, linear Vlasov–Poisson theory predicts an exponential decay of the electric field amplitude at a rate $\gamma_t = -0.151 \omega_{pe}$, which we use as a reference value when assessing the numerical results.

The simulation results for Landau damping are presented in Fig. 5. As shown in Fig. 5(a), the temporal decay of the first Fourier mode of the electric field is in good agreement with the analytical prediction, demonstrating that

the expected Landau damping rate is accurately captured. The absolute value of the total momentum, shown in Fig. 5(b), exhibits small fluctuations during the simulation but remains conserved to within an order of magnitude of $|P| \sim 10^{-3}$ at the final simulation time. Energy conservation is assessed in Fig. 5(c), where we report the absolute relative deviation from the initial energy. After brief initial fluctuations, the energy deviation stabilizes at a level of approximately $|\mathcal{E}(t) - \mathcal{E}(0)|/|\mathcal{E}(0)| \sim 10^{-3}$. Finally, snapshots of the distribution function f at selected times are shown in Fig. 5(d)–(f), clearly illustrating the progressive filamentation characteristic of Landau damping. As time evolution progresses, small negative numerical artifacts develop, with the minimum value reaching $f_{\min} \approx -2 \times 10^{-5}$ after the first time step and increasing gradually to $f_{\min} \approx -4 \times 10^{-4}$ at the final step.

Two-stream instability. We consider the two-stream instability on the domain $x \in [-\pi/3.06, \pi/3.06]$, $v \in [-0.6, 0.6]$. The initial distribution consists of two counter-propagating Maxwellian beams with a superimposed first Fourier-mode spatial perturbation,

$$f(x, v, 0) = (f_+(x, v) + f_-(x, v)) (1 + A \cos(k x)), \quad k = \frac{2\pi}{L_x}, \quad (22)$$

with the beams defined as

$$f_{\pm}(x, v) = \frac{1}{2\sqrt{2\pi}v_{\text{th}}} \exp\left(-\frac{(v \pm v_0)^2}{2v_{\text{th}}^2}\right). \quad (23)$$

In Eqs. (22) and (23), the thermal velocity is $v_{\text{th}} = 0.01$, the perturbation amplitude is $A = 0.01$, and the bulk beam velocity is $v_0 = 0.2$. In the linear regime, this configuration is unstable and exhibits exponential growth of the electric field amplitude. For the parameters used here, linear theory predicts a growth rate $\gamma_t = 0.354\omega_{pe}$ of the first electric field mode.

The simulation results for the two-stream instability are presented in Fig. 6. As shown in Fig. 6(a), the growth rate of the first Fourier mode of the electric field in the linear regime is in excellent agreement with the analytical prediction, confirming that the growth of the instability is accurately captured. The evolution of the conserved quantities is shown in Fig. 6(b) and (c). Both the absolute momentum and the absolute relative energy deviation increase slightly during the linear growth phase and subsequently appear to stabilize once the system enters the nonlinear regime. The maximum deviations attained are approximately $|P| \sim 10^{-3}$ for the momentum

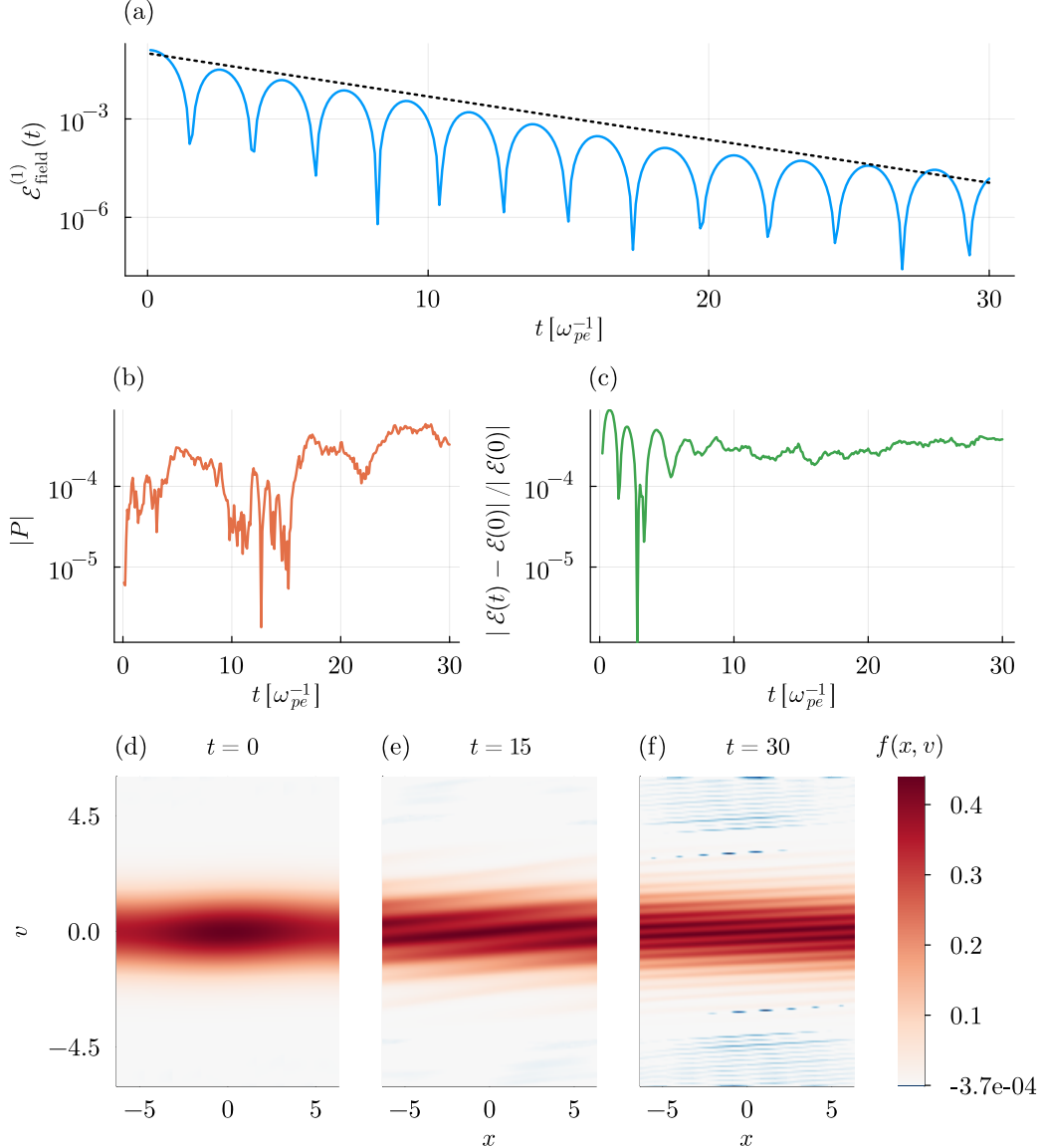


Figure 5: TT-based simulation of Landau damping, with initial condition set according to Eq. (21). **(a)** Energy of first mode of electric field $\mathcal{E}_{\text{field}}^{(1)}$. The analytically computed damping rate is indicated by the dashed line, showing good agreement with the simulated results. **(b–c)** Evolution of absolute momentum $|P|$ and absolute relative energy deviation $|\mathcal{E}(t) - \mathcal{E}(0)|/|\mathcal{E}(0)|$ throughout the simulation. Whereas the momentum appears to fluctuate, the energy conservation quickly stabilizes. **(d–f)** Snapshots of the distribution function f , showing gradual filamentation along the velocity domain.

and $|\mathcal{E}(t) - \mathcal{E}(0)|/|\mathcal{E}(0)| \sim 10^{-2}$ for the energy. Snapshots of the distribution function at selected times are shown in Fig. 6(d)–(f), illustrating the gradual development of the instability and the eventual merging of the two streams at approximately $t \approx 20$. Compared to Landau damping, the negative artifacts of the distribution function are more pronounced but remain localized, reaching a minimum value of $f_{\min} \approx -3.3$ at $t = 20$.

4.2. Effect of tensor-train truncation

In this section, we study the effects of truncating the bond dimension of the TT representation of the distribution function f . We perform a sweep of the TT cutoff error $\epsilon \in \{10^{-7}, 10^{-8}, 10^{-9}, 10^{-10}\}$, keeping the remaining simulation parameters set to the values stated in Table 1. As before, we consider Landau damping and the two-stream instability as our test cases.

In Fig. 7(a) and (b), we show the time evolution of the energy of the first Fourier mode of the electric field, $\mathcal{E}_{\text{field}}^{(1)}$, for Landau damping and the two-stream instability, respectively, as the singular value truncation threshold ϵ is varied. For Landau damping, increasing the truncation error ϵ primarily manifests as a reduction in the damping rate. This effect is most pronounced for $\epsilon = 10^{-7}$, where the decay of $\mathcal{E}_{\text{field}}^{(1)}$ is significantly slower compared to the results obtained with more stringent truncation thresholds. In contrast, no comparable deviations in the electric field energy are observed for the two-stream instability, for which the evolution of $\mathcal{E}_{\text{field}}^{(1)}$ remains nearly identical across all considered cutoff values.

The maximum bond dimensions χ_{\max} attained during the simulations for Landau damping and the two-stream instability are shown in Fig. 7(c) and (d), respectively. As expected, decreasing ϵ leads to a systematic increase in χ_{\max} . For Landau damping, the required bond dimensions remain comparatively modest, with values in the range $15 \lesssim \chi_{\max} \lesssim 45$. In contrast, the two-stream instability exhibits substantially larger bond dimensions, reaching approximately $120 \lesssim \chi_{\max} \lesssim 150$ in the nonlinear regime. Notably, for the two-stream instability, the bond dimension grows steadily throughout the linear phase and then reaches a plateau once the system enters the nonlinear regime. This saturation is a favorable property, as it indicates that the computational cost associated with the TT representation does not increase indefinitely beyond the onset of nonlinear dynamics.

Concerning the phase-space distributions, the observed negative numerical artifacts exhibit a clear and systematic dependence on the truncation level ϵ , indicating that they are directly linked to the low-rank compression of the

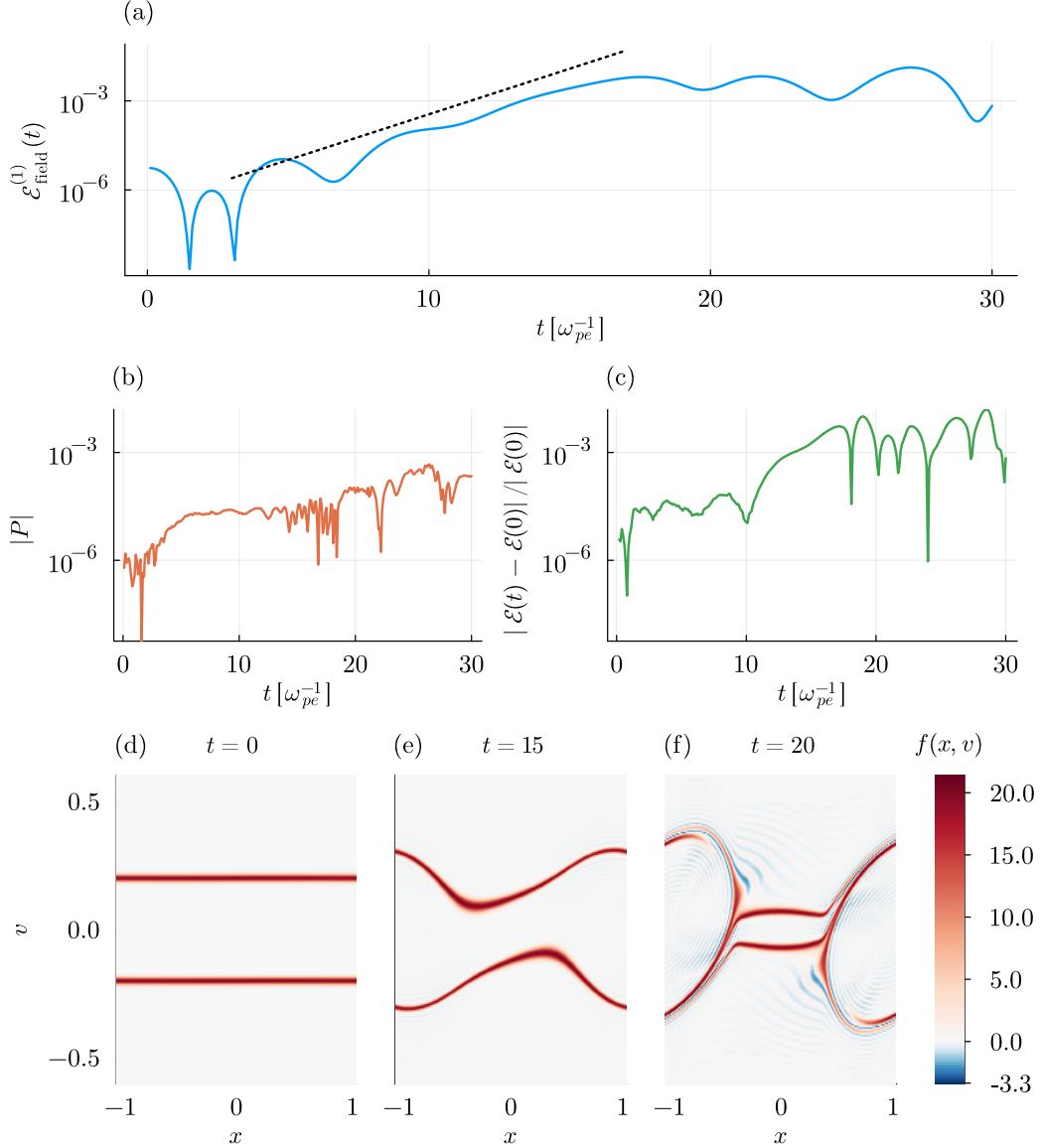


Figure 6: TT-based simulation of two-stream instability, with the initial condition set according to Eq. (22). **(a)** Energy of first mode of electric field. The analytically expected growth rate in the linear regime, indicated by the dotted line, is in excellent agreement with the simulated results. **(b–c)** The absolute momentum $|P|$ and absolute relative energy deviation $|\mathcal{E}(t) - \mathcal{E}(0)| / |\mathcal{E}(0)|$ appear to grow slightly in the linear regime, but show no increasing trend once the system enters the nonlinear regime. **(d–f)** Snapshots of the distribution function throughout time evolution. As expected, we observe the opposing streams gradually couple, until finally merging.

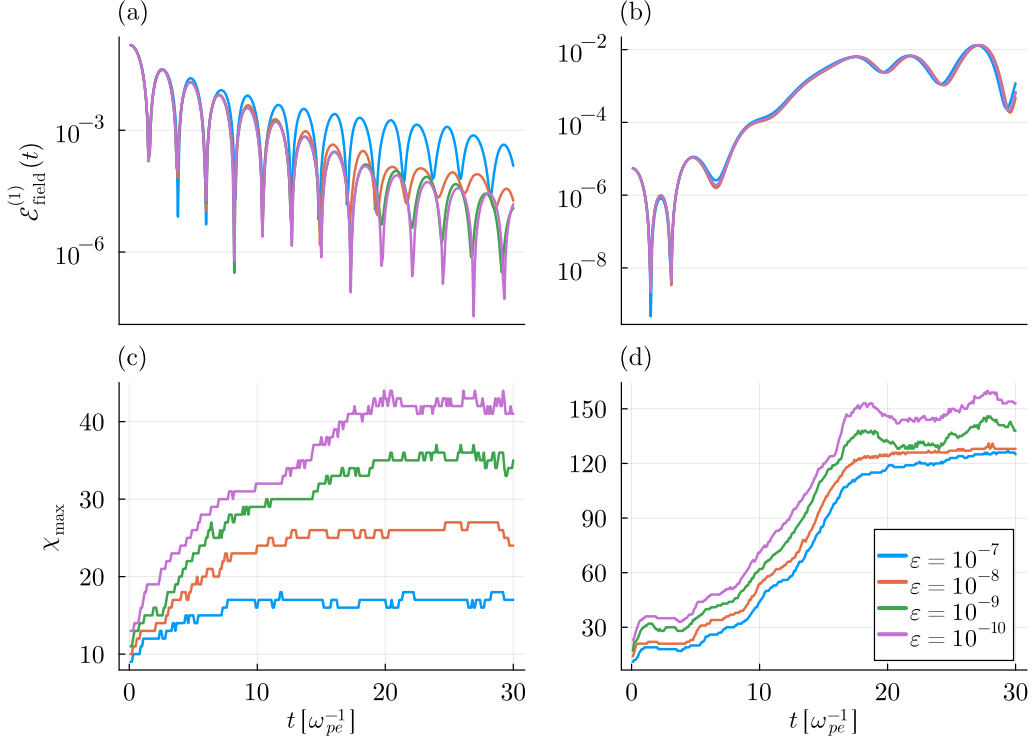


Figure 7: Effects of TT singular value truncation on Landau damping and two-stream instability simulation. **(a–b)** The energy of the first mode of the electric field, $\mathcal{E}_{\text{field}}^{(1)}$, plotted for different values of the TT truncation cutoff ϵ for linear Landau damping and two-stream instability. For the linear Landau damping, increasing the truncation appears to decrease the damping rate of the field energy. **(c–d)** Evolution of maximum bond dimension χ_{\max} for Landau damping and two-stream instability. For the two-stream instability, we observe a clear plateau in the bond dimension growth upon entering the nonlinear regime.

TT representation. In particular, more aggressive truncation makes the negativity more pronounced, as can be observed in Fig. 8. For Landau damping, the minimum value of the distribution function decreases by approximately one order of magnitude from $f_{\min} \approx -3 \times 10^{-4}$ to $f_{\min} \approx -2 \times 10^{-3}$ when increasing the truncation error threshold from $\epsilon = 10^{-10}$ to $\epsilon = 10^{-7}$. A similar trend is observed for the two-stream instability, where the minimum value decreases from approximately $f_{\min} \approx -5$ to $f_{\min} \approx -15$ when varying ϵ in the same range. Importantly, these large negative values remain strongly localized to small, isolated regions of phase space rather than being distributed globally. Strategies for mitigating such negative artifacts and

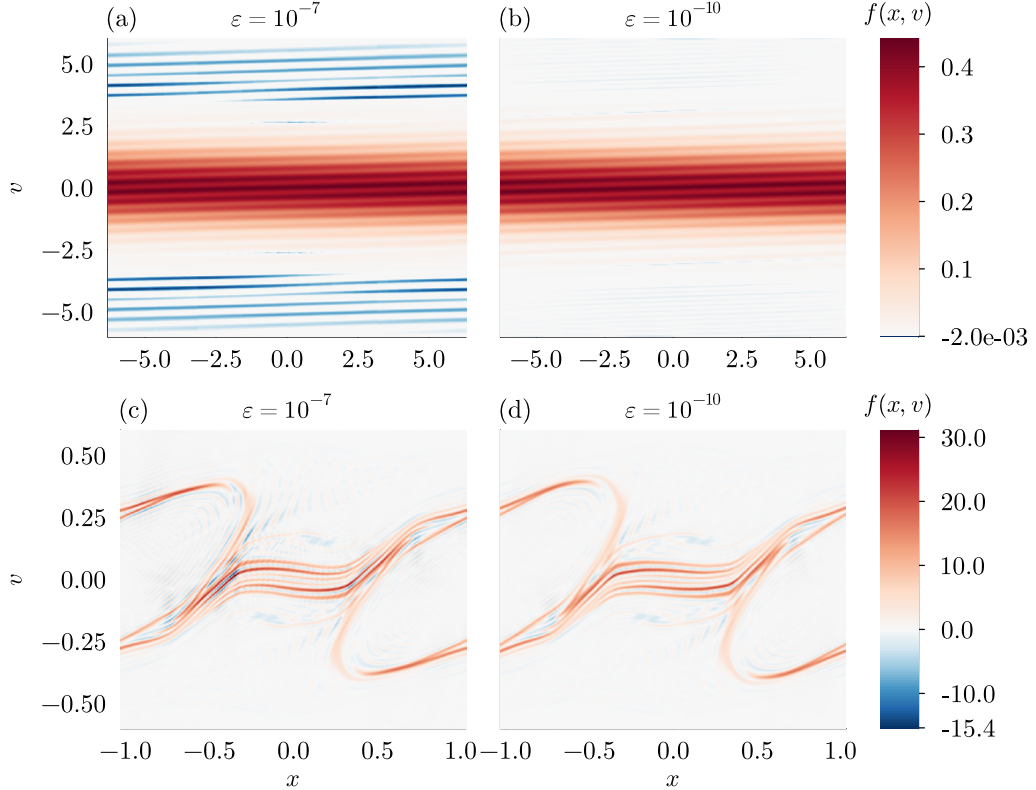


Figure 8: Distribution function of **(a–b)** Landau damping and **(c–d)** two-stream instability using truncation cutoff $\epsilon = 10^{-7}$ and $\epsilon = 10^{-10}$, plotted at the final simulation time $t = 30$. For both Landau damping and the two-stream instability, increasing the aggressiveness of the truncation cutoff ϵ produces larger negative artifacts.

improving positivity preservation are discussed in Section 5.

In Fig. 9, we show the impact of the truncation threshold ϵ on the conservation of momentum and energy. For Landau damping, a modest but systematic improvement in the conservation of both quantities is observed as the TT truncation threshold is decreased. In particular, reducing ϵ from 10^{-7} to 10^{-10} leads to a slight reduction in the final relative energy deviation, $|\mathcal{E}(t) - \mathcal{E}(0)|/|\mathcal{E}(0)|$, from approximately 10^{-3} to $4 \cdot 10^{-4}$ (Fig. 9(a)). A similar improvement is observed for the absolute momentum, $|P|$, which decreases from $2 \cdot 10^{-3}$ to $3 \cdot 10^{-4}$ over the same range of ϵ (Fig. 9(c)). In contrast, no clear dependence on the truncation threshold is observed for the two-stream instability, where the conservation of both energy and momentum remains

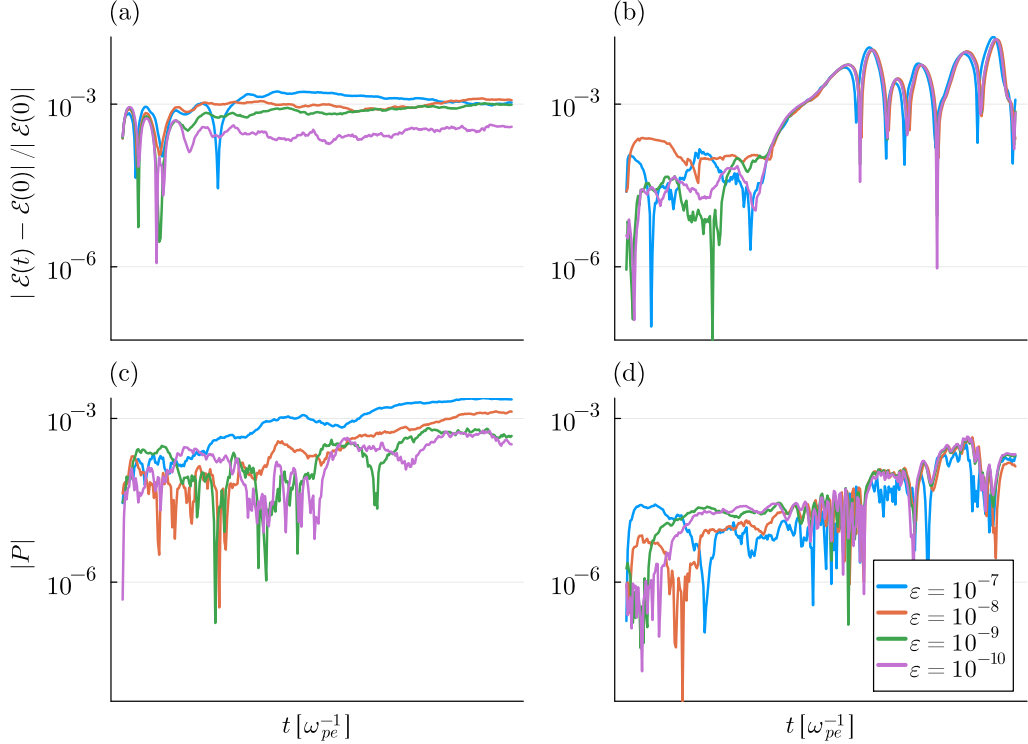


Figure 9: Effects of TT singular value truncation threshold ϵ on conservation of **(a–b)** energy and **(c–d)** momentum. Whereas we find a slight improvement in the conservation properties for Landau damping for smaller truncation thresholds ϵ , the conservation of physical quantities during the two-stream instability generally seems to remain unimpacted by varying the cutoff value within the studied range.

largely unaffected by ϵ within the range of values considered (Fig. 9(b) and (d)).

4.3. Algorithm runtime

Finally, we comment on the algorithm runtime. Table 2 reports the average runtime per integration time step for the Landau damping simulations for different values of the TT truncation threshold ϵ . The runtime is decomposed into the contribution associated with the TCI fit of the accelerated distribution function in Eq. (15) and the combined runtime of all TT–MPO contraction steps. The results show that the TCI fit of the acceleration step induced by the electric field constitutes the dominant computational cost, requiring, on average, approximately one order of magnitude more computational

Table 2: Average runtime \pm STD for (1) TCI fit, (2) TT–MPO contractions, (3) total step when simulating linear Landau damping for different values of the TT truncation cutoff ϵ .

ϵ	TCI [s]	TT–MPO [s]	Total [s]
10^{-7}	1.839 ± 0.590	0.183 ± 0.009	2.038 ± 0.596
10^{-8}	1.705 ± 0.526	0.194 ± 0.013	1.916 ± 0.536
10^{-9}	2.196 ± 0.883	0.209 ± 0.019	2.421 ± 0.899
10^{-10}	2.331 ± 0.819	0.218 ± 0.019	2.565 ± 0.835

time than all TT–MPO contractions combined. Notably, this separation of runtime persists across all considered values of the truncation threshold ϵ , indicating that the relative runtime contribution of the TCI step is largely insensitive to the chosen threshold value. We discuss means of improving performance in Section 5.

5. Discussion

The results presented in this work indicate that a combination of a quantics TT-based representation of the distribution function f with a spectral based solver, utilizing the MPO representation of the Fourier transform, yields promising results and successfully reproduces several important features characteristic of collisionless plasmas, including the analytic damping rate of Landau damping and the growth rate of the linear regime of the two-stream instability. In both the Landau damping and two-stream instability simulations, the solver demonstrated robust conservation behavior, with momentum and energy remaining well preserved throughout the time evolution, generally exhibiting limited drift over time despite dynamic bond dimension adaptation and repeated truncation.

As bond dimension truncation of the TT is crucial in keeping the TT-based simulations computationally feasible, it is important to understand the impact of the truncations on the physical properties of the system. In our simulations of the two-stream instability, the evolution of the electric field energy, as well as the conservation of charge and momentum, remained largely unaffected by variations in the bond dimension cutoff within the range considered. While this does not constitute conclusive evidence, it suggests that macroscopic observables derived from the distribution function f may be robust to TT truncations. A more systematic investigation is, however,

required to better understand the relationship between TT bond dimension truncation and its direct impact on the physical properties of the system. In future work, we believe that further improvements to conservation properties could be achieved by incorporating projection-based correction schemes, such as the method proposed by Kormann [19], in which the TT state representation is repeatedly projected onto the manifold of distributions with fixed mass and momentum, at the cost of a modest increase in bond dimension.

A current limitation of the proposed method is the emergence of negative numerical artifacts in the distribution function, which become increasingly pronounced under more aggressive bond dimension truncation. This is a common issue in Vlasov solvers, which is usually addressed via positivity preserving schemes [50]. One promising direction for mitigating this issue, within the TT framework, is to represent the square root of the distribution function, \sqrt{f} , rather than f itself. This idea has recently been proposed in a non-TT context as a means of enforcing positivity by construction [51]. From a conceptual standpoint, such a formulation is closer in spirit to quantum simulations and quantum-inspired tensor network methods, where one represents an underlying amplitude while physically relevant observables are obtained only after taking suitable quadratic forms. Moreover, since SVD-based truncation is optimal with respect to the L^2 norm, whereas the physically relevant norm for f is the L^1 norm, a square-root formulation may lead to truncations that more faithfully preserve key physical properties of the system.

Concerning performance, we found that the TCI step used to fit the accelerated distribution dominated the overall runtime. This is partially explained by the intrinsic complexity of the interpolation task, which requires fitting a TT representation over the combined position and velocity registers. In addition, each TCI query of the accelerated-state in Eq. (15) is computationally expensive, as it involves evaluating both the electric field $E(x_{i_x})$ and the current distribution function $\hat{f}(x_{i_x}, k_{i_v})$ through separate TT contractions. This cost could be partially mitigated by caching previously evaluated queries to avoid redundant sampling and by leveraging GPU acceleration for the tensor contractions involved in query evaluation. Further performance improvements may be obtained by exploiting shared-memory parallelization strategies, such as those proposed in [47], as well as by systematically exploring the impact of different TCI algorithmic variants, including single- and two-site updates and alternative pivot-exploration strategies, on overall efficiency [44]. Furthermore, it may be worthwhile to consider alternative bit-

ordering schemes beyond the interleaved ordering, as was explored in [39]. This question is particularly relevant in the present setting, as the MPO representation of the Fourier transform reverses the quantics bit order of the transformed register, thereby partially breaking the original interleaved ordering between position and velocity. Whether alternative bit-ordering schemes can better accommodate such transformations or simplify the TCI interpolation remains an interesting direction for future investigation.

A natural extension of the present framework is the treatment of higher-dimensional systems. At the representation level, a D -dimensional distribution function $f(\mathbf{x}, \mathbf{v})$ can be incorporated into the TT format by introducing additional quantics bit-registers for each spatial and velocity component, increasing the TT order from $2R$ to $2DR$. The numerical efficiency of such an extension, however, critically depends on whether a compact low-rank TT representation can be maintained as the dimensionality increases. Encouragingly, early work on TT-based Vlasov–Poisson solvers suggests that low-rank representations of the distribution function can remain viable even in higher-dimensional settings [19].

Before concluding, it is useful to place the TT truncation employed here in the broader context of closures used throughout plasma physics to render high-dimensional descriptions tractable. In kinetic theory, the BBGKY hierarchy organizes particle correlations, and practical models such as the Vlasov or Boltzmann equations are obtained by closing the hierarchy under assumptions appropriate to a given regime [52, 53]. Similarly, fluid and MHD models follow from taking velocity moments of the kinetic equations and introducing closures that truncate the resulting infinite moment hierarchy [54, 55]. The quantics TT formulation introduces a different notion of closure. Rather than truncating particle correlations or moment equations, TT truncation limits complexity by restricting the rank of a tensorized representation of f , thereby weakening inter-scale couplings in the quantics hierarchy. Practically, this is realized by discarding low-weight singular values, which adaptively compresses the state while preserving its dominant separable structure. In this sense, TT truncation serves an analogous purpose to classical closures, controlling complexity while acting on the numerical representation instead of imposing an explicit physical approximation.

6. Conclusion

In this work, we have presented a spectral solver for the collisionless Vlasov–Poisson system that represents the phase-space distribution function f in a quantics TT format and advances the dynamics in compressed form without full-grid reconstruction. A central idea of the method is that spectral operations are executed directly within the tensor network representation, as Fourier transforms are applied via TT–MPO contractions. The self-consistent electric field is obtained from tensor contractions that extract the required velocity moments without reconstructing f on a full grid. In this way, the method addresses a main bottleneck of Eulerian kinetic solvers, namely the storage and manipulation of high-dimensional phase-space data, by evolving the solution directly in a low-rank tensor network state. We validated the method on standard benchmarks, including linear Landau damping and the two-stream instability, where the solver reproduces the expected damping and growth rates of the electric field. Beyond benchmark verification, we systematically investigated the impact of compression through variations of truncation tolerances and internal ranks (bond dimensions) on momentum and energy conservation, positivity behavior, robustness under filamentation, and overall computational cost. These studies clarify the regimes in which compression can be achieved while preserving the fidelity of the resulting physics.

At the same time, important open questions remain. In particular, further work is needed to characterize truncation effects more comprehensively across longer integration times and more strongly nonlinear regimes, and to develop diagnostics that reliably predict when compressibility deteriorates [56, 57]. In addition, in our current implementation, the repeated TCI reconstructions required for the acceleration substep constitute the dominant computational cost, motivating future work on more efficient update strategies, improved interpolation and query policies, and performance optimizations [58, 59]. Extending the framework to higher-dimensional settings and to electromagnetic models such as Vlasov–Maxwell, while retaining fully compressed operator application, is another natural direction for future work [8]. Overall, our results support the view that tensor network compression can be used not only for storage but also as a computational representation in which kinetic equations are advanced directly, making spectral tensor network solvers a promising route toward high-accuracy Eulerian Vlasov simulations.

7. Data availability

The code and data used to generate the numerical results presented in this work are available in the public repository `VlasovTT.jl` [60].

Acknowledgements

This work is funded by the European Union. This work has received funding from the European High Performance Computing Joint Undertaking (JU) and Sweden, Finland, Germany, Greece, France, Slovenia, Spain, and the Czech Republic under grant agreement No. 101093261, Plasma-PEPSC.

References

- [1] R. M. Kulsrud, Plasma Physics for Astrophysics, Princeton University Press, Princeton, NJ, 2005.
- [2] R. D. Hazeltine, J. D. Meiss, Plasma Confinement, Dover Publications, Mineola, NY, 2003.
- [3] F. F. Chen, Introduction to Plasma Physics and Controlled Fusion, 3rd Edition, Springer, Cham, 2016. doi:10.1007/978-3-319-22309-4.
- [4] J. P. Goedbloed, S. Poedts, Principles of Magnetohydrodynamics: With Applications to Laboratory and Astrophysical Plasmas, Cambridge University Press, Cambridge, 2004. doi:10.1017/CBO9780511616945.
- [5] M. Goossens, An Introduction to Plasma Astrophysics and Magnetohydrodynamics, Vol. 294 of Astrophysics and Space Science Library, Springer Netherlands, Dordrecht, 2003. doi:10.1007/978-94-007-1076-4.
URL <http://link.springer.com/10.1007/978-94-007-1076-4>
- [6] D. R. Nicholson, Introduction to Plasma Theory, Wiley Series in Plasma Physics, John Wiley & Sons, New York, NY, USA, 1983.
- [7] R. E. Heath, I. M. Gamba, P. J. Morrison, C. Michler, A discontinuous Galerkin method for the Vlasov–Poisson system, Journal of Computational Physics 231 (4) (2012) 1140–1174. doi:10.1016/j.jcp.2011.09.020.
URL <https://www.sciencedirect.com/science/article/pii/S0021999111005523>

- [8] L. Einkemmer, A. Ostermann, C. Piazzola, A low-rank projector-splitting integrator for the Vlasov–Maxwell equations with divergence correction, *Journal of Computational Physics* 403 (2020) 109063. doi:10.1016/j.jcp.2019.109063.
 URL <https://www.sciencedirect.com/science/article/pii/S0021999119307685>
- [9] E. Sonnendrücker, J. Roche, P. Bertrand, A. Ghizzo, The Semi-Lagrangian Method for the Numerical Resolution of the Vlasov Equation, *Journal of Computational Physics* 149 (2) (1999) 201–220. doi:10.1006/jcph.1998.6148.
 URL <https://www.sciencedirect.com/science/article/pii/S0021999198961484>
- [10] F. Filbet, E. Sonnendrücker, P. Bertrand, Conservative Numerical Schemes for the Vlasov Equation, *Journal of Computational Physics* 172 (1) (2001) 166–187. doi:10.1006/jcph.2001.6818.
 URL <https://linkinghub.elsevier.com/retrieve/pii/S0021999101968184>
- [11] L. Einkemmer, I. Joseph, A mass, momentum, and energy conservative dynamical low-rank scheme for the Vlasov equation, *Journal of Computational Physics* 443 (2021) 110495. doi:10.1016/j.jcp.2021.110495.
 URL <https://www.sciencedirect.com/science/article/pii/S0021999121003909>
- [12] M. Gutnic, M. Haefele, I. Paun, E. Sonnendrücker, Vlasov simulations on an adaptive phase-space grid, *Computer Physics Communications* 164 (1) (2004) 214–219. doi:10.1016/j.cpc.2004.06.073.
 URL <https://www.sciencedirect.com/science/article/pii/S0010465504002838>
- [13] J. A. F. Hittinger, J. W. Banks, Block-structured adaptive mesh refinement algorithms for Vlasov simulation, *Journal of Computational Physics* 241 (2013) 118–140. doi:10.1016/j.jcp.2013.01.030.
 URL <https://www.sciencedirect.com/science/article/pii/S0021999113000740>
- [14] L. Einkemmer, C. Lubich, A Low-Rank Projector-Splitting Integrator for the Vlasov–Poisson Equation, *SIAM Journal on Scientific Computing*

- 40 (5) (2018) B1330–B1360. doi:10.1137/18M116383X.
 URL <https://pubs.siam.org/doi/10.1137/18M116383X>
- [15] C. K. Birdsall, A. B. Langdon, *Plasma Physics via Computer Simulation*, McGraw-Hill, New York, 1985.
- [16] R. W. Hockney, J. W. Eastwood, *Computer Simulation Using Particles*, Taylor & Francis, 1988.
- [17] O. Koch, C. Lubich, *Dynamical Low-Rank Approximation*, SIAM Journal on Matrix Analysis and Applications 29 (2) (2007) 434–454. doi:10.1137/050639703.
 URL <https://pubs.siam.org/doi/10.1137/050639703>
- [18] I. V. Oseledets, *Tensor-Train Decomposition*, SIAM Journal on Scientific Computing 33 (5) (2011) 2295–2317, publisher: Society for Industrial and Applied Mathematics. doi:10.1137/090752286.
 URL <https://pubs.siam.org/doi/10.1137/090752286>
- [19] K. Kormann, *A Semi-Lagrangian Vlasov Solver in Tensor Train Format*, SIAM Journal on Scientific Computing 37 (4) (2015) B613–B632, publisher: Society for Industrial and Applied Mathematics. doi:10.1137/140971270.
 URL <https://pubs.siam.org/doi/10.1137/140971270>
- [20] N. Gourianov, M. Lubasch, S. Dolgov, Q. Y. v. d. Berg, H. Babaee, P. Givi, M. Kiffner, D. Jaksch, *A Quantum Inspired Approach to Exploit Turbulence Structures*, Nature Computational Science 2 (1) (2022) 30–37, arXiv:2106.05782 [physics]. doi:10.1038/s43588-021-00181-1.
 URL <http://arxiv.org/abs/2106.05782>
- [21] H. Ishida, N. Okada, S. Hoshino, H. Shinaoka, *Low-Rank Quantics Tensor Train Representations of Feynman Diagrams for Multiorbital Electron-Phonon Models*, Physical Review Letters 135 (4) (2025) 046502, publisher: American Physical Society. doi:10.1103/tkcp-p5br.
 URL <https://link.aps.org/doi/10.1103/tkcp-p5br>
- [22] S. V. Dolgov, A. P. Smirnov, E. E. Tyrtyshnikov, *Low-rank approximation in the numerical modeling of the Farley–Buneman instability*

- in ionospheric plasma, *Journal of Computational Physics* 263 (2014) 268–282. doi:10.1016/j.jcp.2014.01.029.
URL <https://www.sciencedirect.com/science/article/pii/S0021999114000564>
- [23] M. Niedermeier, A. Moulinas, T. Louvet, J. L. Lado, X. Waintal, Solving the Gross-Pitaevskii equation on multiple different scales using the quantics tensor train representation, arXiv:2507.04262 [quant-ph] (Jul. 2025). doi:10.48550/arXiv.2507.04262.
URL <http://arxiv.org/abs/2507.04262>
- [24] K. J. Woolfe, C. D. Hill, L. C. L. Hollenberg, Scale invariance and efficient classical simulation of the quantum Fourier transform, arXiv:1406.0931 [quant-ph] (Jun. 2014). doi:10.48550/arXiv.1406.0931.
URL <http://arxiv.org/abs/1406.0931>
- [25] J. Chen, E. Stoudenmire, S. R. White, Quantum Fourier Transform Has Small Entanglement, *PRX Quantum* 4 (4) (2023) 040318. doi:10.1103/PRXQuantum.4.040318.
URL <https://link.aps.org/doi/10.1103/PRXQuantum.4.040318>
- [26] G. Vidal, Efficient Classical Simulation of Slightly Entangled Quantum Computations, *Physical Review Letters* 91 (14) (2003) 147902. doi:10.1103/PhysRevLett.91.147902.
URL <https://link.aps.org/doi/10.1103/PhysRevLett.91.147902>
- [27] G. Vidal, Efficient Simulation of One-Dimensional Quantum Many-Body Systems, *Physical Review Letters* 93 (4) (2004) 040502. doi:10.1103/PhysRevLett.93.040502.
URL <https://link.aps.org/doi/10.1103/PhysRevLett.93.040502>
- [28] U. Schollwoeck, The density-matrix renormalization group in the age of matrix product states, *Annals of Physics* 326 (1) (2011) 96–192, arXiv:1008.3477 [cond-mat]. doi:10.1016/j.aop.2010.09.012.
URL <http://arxiv.org/abs/1008.3477>
- [29] R. Orus, A Practical Introduction to Tensor Networks: Matrix Product States and Projected Entangled Pair States, *Annals of Physics* 349 (2014) 117–158, arXiv:1306.2164 [cond-mat]. doi:10.1016/j.aop.

2014.06.013.

URL <http://arxiv.org/abs/1306.2164>

- [30] J. Brandejs, N. Hörnblad, E. F. Valeev, A. Heinecke, J. Hammond, D. Matthews, P. Bientinesi, Tensor Algebra Processing Primitives (TAPP): Towards a Standard for Tensor Operations, arXiv:2601.07827 [cs] (Jan. 2026). doi:10.48550/arXiv.2601.07827.
URL <http://arxiv.org/abs/2601.07827>
- [31] G. Manzini, T. Sorgente, The low-rank tensor-train finite difference method for three-dimensional parabolic equations, Mathematics and Computers in Simulation 241 (2026) 591–616. doi:<https://doi.org/10.1016/j.matcom.2025.08.027>.
URL <https://www.sciencedirect.com/science/article/pii/S0378475425003702>
- [32] B. N. Khoromskij, Tensor Numerical Methods for High-dimensional PDEs: Basic Theory and Initial Applications, arXiv:1408.4053 [math] (Aug. 2014). doi:10.48550/arXiv.1408.4053.
URL <http://arxiv.org/abs/1408.4053>
- [33] B. N. Khoromskij, Tensors-structured numerical methods in scientific computing: Survey on recent advances, Chemometrics and Intelligent Laboratory Systems 110 (1) (2012) 1–19. doi:10.1016/j.chemolab.2011.09.001.
URL <https://www.sciencedirect.com/science/article/pii/S0169743911001808>
- [34] R. D. Peddinti, S. Pisoni, A. Marini, P. Lott, H. Argentieri, E. Tiunov, L. Aolita, Quantum-inspired framework for computational fluid dynamics, Communications Physics 7 (1) (2024) 135. doi:10.1038/s42005-024-01623-8.
URL <https://www.nature.com/articles/s42005-024-01623-8>
- [35] L. Hölscher, P. Rao, L. Müller, J. Klepsch, A. Luckow, T. Stollenwerk, F. K. Wilhelm, Quantum-inspired fluid simulation of two-dimensional turbulence with GPU acceleration, Physical Review Research 7 (1) (2025) 013112, publisher: American Physical Society. doi:10.1103/PhysRevResearch.7.013112.

URL <https://link.aps.org/doi/10.1103/PhysRevResearch.7.013112>

- [36] N. Gourianov, P. Givi, D. Jaksch, S. B. Pope, Tensor networks enable the calculation of turbulence probability distributions, *Science Advances* 11 (5) (2025) eads5990. doi:10.1126/sciadv.ads5990.
URL <https://www.science.org/doi/10.1126/sciadv.ads5990>
- [37] S. V. Dolgov, B. N. Khoromskij, I. V. Oseledets, Fast Solution of Parabolic Problems in the Tensor Train/Quantized Tensor Train Format with Initial Application to the Fokker–Planck Equation, *SIAM Journal on Scientific Computing* 34 (6) (2012) A3016–A3038, publisher: Society for Industrial and Applied Mathematics. doi:10.1137/120864210.
URL <https://pubs.siam.org/doi/10.1137/120864210>
- [38] D. P. Truong, M. I. Ortega, I. Boureima, G. Manzini, K. Ø. Rasmussen, B. S. Alexandrov, Tensor networks for solving the time-independent boltzmann neutron transport equation, *Journal of Computational Physics* 507 (2024) 112943. doi:<https://doi.org/10.1016/j.jcp.2024.112943>.
URL <https://www.sciencedirect.com/science/article/pii/S002199912400192X>
- [39] E. Ye, N. F. G. Loureiro, Quantum-inspired method for solving the Vlasov-Poisson equations, *Physical Review E* 106 (3) (2022) 035208, publisher: American Physical Society. doi:10.1103/PhysRevE.106.035208.
URL <https://link.aps.org/doi/10.1103/PhysRevE.106.035208>
- [40] F. Allmann-Rahn, R. Grauer, K. Kormann, A Parallel Low-Rank Solver for the Six-Dimensional Vlasov-Maxwell Equations, *Journal of Computational Physics* 469 (2022) 111562, arXiv:2201.03471 [physics]. doi:10.1016/j.jcp.2022.111562.
URL <http://arxiv.org/abs/2201.03471>
- [41] E. Ye, N. Loureiro, Quantized tensor networks for solving the Vlasov-Maxwell equations, arXiv:2311.07756 [physics] (Jun. 2024). doi:10.48550/arXiv.2311.07756.
URL <http://arxiv.org/abs/2311.07756>

- [42] G. Strang, On the Construction and Comparison of Difference Schemes, *SIAM Journal on Numerical Analysis* 5 (3) (1968) 506–517, publisher: Society for Industrial and Applied Mathematics. doi:10.1137/0705041.
 URL <https://pubs.siam.org/doi/10.1137/0705041>
- [43] I. Oseledets, E. Tyrtyshnikov, TT-cross approximation for multidimensional arrays, *Linear Algebra and its Applications* 432 (1) (2010) 70–88. doi:10.1016/j.laa.2009.07.024.
 URL <https://www.sciencedirect.com/science/article/pii/S0024379509003747>
- [44] Y. N. Fernández, M. K. Ritter, M. Jeannin, J.-W. Li, T. Kloss, T. Louvet, S. Terasaki, O. Parcollet, J. v. Delft, H. Shinaoka, X. Waintal, Learning tensor networks with tensor cross interpolation: new algorithms and libraries, *SciPost Physics* 18 (3) (2025) 104, arXiv:2407.02454 [physics]. doi:10.21468/SciPostPhys.18.3.104.
 URL <http://arxiv.org/abs/2407.02454>
- [45] C. Z. Cheng, G. Knorr, The integration of the vlasov equation in configuration space, *Journal of Computational Physics* 22 (3) (1976) 330–351. doi:10.1016/0021-9991(76)90053-X.
 URL <https://www.sciencedirect.com/science/article/pii/002199917690053X>
- [46] B. N. Khoromskij, O(dlogN)-Quantics Approximation of N-d Tensors in High-Dimensional Numerical Modeling, *Constructive Approximation* 34 (2) (2011) 257–280. doi:10.1007/s00365-011-9131-1.
 URL <https://doi.org/10.1007/s00365-011-9131-1>
- [47] S. Dolgov, D. Savostyanov, Parallel cross interpolation for high-precision calculation of high-dimensional integrals, *Computer Physics Communications* 246 (2020) 106869, publisher: North-Holland. doi:10.1016/j.cpc.2019.106869.
 URL <https://www.sciencedirect.com/science/article/pii/S0010465519302565>
- [48] S. Paeckel, T. Köhler, A. Swoboda, S. R. Manmana, U. Schollwöck, C. Hubig, Time-evolution methods for matrix-product states, *Annals of Physics* 411 (2019) 167998. doi:10.1016/j.aop.2019.167998.

URL <https://www.sciencedirect.com/science/article/pii/S0003491619302532>

- [49] M. Fishman, S. R. White, E. M. Stoudenmire, The ITensor Software Library for Tensor Network Calculations, *SciPost Phys. Codebases* (2022) 4Publisher: SciPost. doi:10.21468/SciPostPhysCodeb.4.
URL <https://scipost.org/10.21468/SciPostPhysCodeb.4>
- [50] Y. Kiechle, E. Chudzik, C. Helzel, A positivity-preserving Active Flux method for the Vlasov-Poisson system, *Journal of Computational Physics* 524 (2025) 113693. doi:10.1016/j.jcp.2024.113693.
URL <https://www.sciencedirect.com/science/article/pii/S0021999124009410>
- [51] O. Issan, O. Koshkarov, F. D. Halpern, B. Kramer, G. L. Delzanno, Anti-symmetric and positivity preserving formulation of a spectral method for Vlasov-Poisson equations, *Journal of Computational Physics* 514 (2024) 113263. doi:10.1016/j.jcp.2024.113263.
URL <https://www.sciencedirect.com/science/article/pii/S0021999124005114>
- [52] S. Ichimaru, *Statistical Plasma Physics, Volume I: Basic Principles*, CRC Press, 2004. doi:10.1201/9780429497155.
- [53] R. Balescu, *Statistical Mechanics of Charged Particles*, Interscience Publishers, 1963.
- [54] H. Grad, On the kinetic theory of rarefied gases, *Communications on Pure and Applied Mathematics* 2 (4) (1949) 331–407, _eprint: <https://onlinelibrary.wiley.com/doi/pdf/10.1002/cpa.3160020403>. doi:10.1002/cpa.3160020403.
URL <https://onlinelibrary.wiley.com/doi/abs/10.1002/cpa.3160020403>
- [55] C. D. Levermore, Moment closure hierarchies for kinetic theories, *Journal of Statistical Physics* 83 (5) (1996) 1021–1065. doi:10.1007/BF02179552.
URL <https://doi.org/10.1007/BF02179552>

- [56] J. Kusch, L. Einkemmer, G. Ceruti, On the Stability of Robust Dynamical Low-Rank Approximations for Hyperbolic Problems, *SIAM Journal on Scientific Computing* 45 (1) (2023) A1–A24. [doi:10.1137/21M1446289](https://doi.org/10.1137/21M1446289)
 URL <https://epubs.siam.org/doi/10.1137/21M1446289>
- [57] L. Einkemmer, K. Kormann, J. Kusch, R. G. McClarren, J.-M. Qiu, A review of low-rank methods for time-dependent kinetic simulations, *Journal of Computational Physics* 538 (2025) 114191. [doi:10.1016/j.jcp.2025.114191](https://doi.org/10.1016/j.jcp.2025.114191).
 URL <https://www.sciencedirect.com/science/article/pii/S0021999125004747>
- [58] D. Savostyanov, I. Oseledets, Fast adaptive interpolation of multi-dimensional arrays in tensor train format, in: *The 2011 International Workshop on Multidimensional (nD) Systems*, 2011, pp. 1–8. [doi:10.1109/nDS.2011.6076873](https://doi.org/10.1109/nDS.2011.6076873).
 URL <https://ieeexplore.ieee.org/document/6076873>
- [59] J. Kusch, Second-order robust parallel integrators for dynamical low-rank approximation, *BIT Numerical Mathematics* 65 (3) (2025) 31. [doi:10.1007/s10543-025-01073-w](https://doi.org/10.1007/s10543-025-01073-w).
 URL <https://doi.org/10.1007/s10543-025-01073-w>
- [60] Github repository - VlasovTT.jl (2026).
 URL <https://github.com/erikasgrim/VlasovTT.jl>